

18. Weinberger DR, Jones D, Reba RC, et al. A comparison of FDG PET and IQNB SPECT in normal subjects and in patients with dementia. *J Neuropsych Clin Neurosci* 1992;4:239–248.
19. Weinberger DR, Jones DW, Sunderland T, et al. In vivo imaging of cerebral muscarinic receptors with iodine-123-QNB and SPECT: studies in normal subjects and patients with dementia. *Clin Neuropharmacol* 1992;15:194A–195A.
20. Wyper DJ, Brown D, Patterson J, et al. Deficits in iodine-labeled 3-quinuclidinyl benzilate binding in relation to cerebral blood flow in patients with Alzheimer's disease. *Eur J Nucl Med* 1993;20:379–386.
21. Sunderland T, Esposito G, Molchan SE, et al. Differential cholinergic regulation in Alzheimer's patients compared to controls following chronic blockade with scopolamine: a SPECT study. *Psychopharmacol* 1995;121:231–241.
22. Lee KS, Gibson RE, Eckelman WC, Reba RC. Radioiodination of a 3-quinuclidinyl benzilate using no-carrier-added concentration of iodine-125/NaI [Abstract]. *J Nucl Med* 1986;27(suppl):1045P.
23. Rzeszutowski WJ, Eckelman WC, Francis BE, et al. Synthesis and evaluation of radioiodinated derivatives of 1-azabicyclo[2.2.2]oct-3-yl alpha-hydroxy-alpha-(4-iodophenyl)-alpha-phenylacetate as potential radiopharmaceuticals. *J Med Chem* 1984;27:156–160.
24. Cohen VI, Rzeszutowski WJ, Gibson RE, Fan LH, Reba RC. Preparation and properties of (R)-(-)-1-azabicyclo[2.2.2]oct-3-yl- (R)-(+)-alpha-hydroxy-alpha-(4-[¹²⁵I]iodophenyl)-alpha-phenyl acetate and (R)-(-)-1-azabicyclo[2.2.2]oct-3-yl-(S)-(-)-alpha-hydroxy-alpha-(4-[¹²⁵I]iodophenyl)-alpha-phenyl acetate as potential radiopharmaceuticals. *J Pharm Sci* 1989;78:833–836.
25. Owens J, Murray T, McCulloch J, Wyper D. Synthesis of (R,R)-¹²³I-QNB, a SPECT agent for cerebral muscarinic acetylcholine receptors in vivo. *J Lab Comp Radiopharm* 1991;31:45–60.
26. Kabalka GW, Gai YZ, Mathur S. Synthesis of iodine-125-labeled 3-quinuclidinyl 4'-iodobenzilate. *Int J Rad Appl Instrum [b]* 1989;16:359–360.

Monte Carlo-Based Analysis of PET Scatter Components

Lars-Eric Adam, Matthias E. Bellemann, Gunnar Brix and Walter J. Lorenz
Radiological Diagnostics and Therapy, German Cancer Research Center, Heidelberg, Germany

This study quantifies the different scatter components in PET and examines how the different components degrade reconstructed PET images. **Methods:** We simulated the measurement of various phantoms using Monte Carlo (MC) calculations and compared the MC-generated projections and images with the corresponding experimental data. The coincidences were subdivided in four classes: primaries, object scatter (scattered in the object only), gantry scatter (scattered in the scanner only) and mixed scatter (scattered both in the object and the scanner). **Results:** In the projections of the line sources, the gantry scatter was closely located around the source position, whereas the object scatter was smeared over the whole field of view and could be parameterized well by a monoexponential function. The mixed scatter had nearly the same distribution as the object scatter, but with a smaller amplitude. The calculations and experimental data were in excellent agreement; i.e., led to the same parameterization of the scatter distribution functions and to a similar localization of the scatter components in the reconstructed images. **Conclusion:** The spatial distribution of the scatter components justifies the widely-used assumption that it is sufficient to restrict experimental scatter correction techniques to the object scatter. Furthermore, it is possible to derive the parameters for the scatter kernels, which are needed for the convolution-subtraction algorithm, by MC simulations.

Key Words: PET; scatter components; scatter correction; Monte Carlo simulations

J Nucl Med 1996; 37:2024–2029

The strength of PET is its ability to quantify the activity distribution of radionuclides in the human body. The accuracy of the quantification, however, critically depends upon the adequate correction of the raw data. Major corrections concern the detector efficiency, the dead time, the random coincidences, the scattered radiation and the attenuation in the object. Scatter correction is mandatory, particularly in abdominal imaging. Without scatter correction, the regional activity accumulation can be under- or overestimated and, thus, may lead to false medical interpretations (1).

Our study is focused on the differentiation of the scatter components that result from the object and the gantry. Based on these data, we try to answer the questions as to where the scatter process takes place, which components are dominant, and how they contribute to the images. A powerful tool for such examinations is the Monte Carlo (MC) technique, which simulates real experiments on the computer and distinguishes the coincidences in the desired way. The direct comparison of the simulations with experiments serves as a cross check.

Several studies have been published that address MC simulations of the scatter process in PET (2–7). They concern scatter in small animal PET systems (3–5) as well as in whole-body tomographs (6), and include studies that use the MC simulation as a basis for a PET simulation program (7). It is therefore well known how the total scatter contributes to the projections of the measured data. Due to limited computer power available in the past, however, these studies had large statistical errors.

Our study extends the MC simulations to a whole-body tomograph with count numbers that are in the order of the measured data. This makes it possible to reconstruct images of the different scatter components and to deduce the parameters of the scatter kernels from the simulations. These data are needed in scatter-correction algorithms, such as the convolution-subtraction technique (8,9).

MATERIALS AND METHODS

PET System

The measurements and simulations were performed for a whole-body PET system (PC 2048–7WB, Scanditronix AB, Uppsala, Sweden). It is a two-ring system with alternating BGO (Bi₄Ge₃O₁₂) and GSO (Gd₂SiO₅) detector crystals of 6 × 20 × 30 mm³. The detector rings are separated by a 5-mm thick lead septum. With the two rings, three slices (two direct and one cross plane) are imaged simultaneously. The patient port diameter is 57 cm, the transaxial field of view (FOV) is 52 cm, and the axial FOV is 4.5 cm. The in-plane resolution in the stationary mode is 6.3 mm in the center of the tomograph and 8.2 mm at a radial distance of 20 cm from the center (10).

Received Nov. 11, 1995; revision accepted March 3, 1996.

For correspondence or reprints contact: Lars-Eric Adam, MSc, PET Research Group, Radiological Diagnostics and Therapy, German Cancer Research Center (dkfz), Im Neuenheimer Feld 280, D-69120 Heidelberg, Germany.

Phantoms and Sources

Quantitative MC and experimental data were obtained by simulating and imaging cylindrical phantoms with diameters ranging from 5 cm to 40 cm and the EEC body phantom (11). The cylinder phantoms had a length of 20 cm and were filled with either water or a homogeneous activity distribution. The line sources were positioned in the water containers with their axes adjusted parallel to the axis of the tomograph. The EEC body phantom (with arms) contained three cylindrical inserts with different fillings (see Fig. 3A for geometrical arrangement and activity data). The EEC body phantom was lying on the couch of the PET scanner in order to mimic the clinical situation, while the cylinder phantoms were placed in the FOV of the PET system without using the couch.

Convolution-Subtraction Method

This well-established scatter correction method in PET was originally proposed by King et al. (8) and evaluated by Bergström et al. (9). The purpose is to improve the image quality through a subtraction of the scattered events. The measured projection data $P_m(x)$ are split in the sum of unscattered and scattered events: $P_m(x) = P(x) + S(x)$. The scatter $S(x)$ can be considered as the convolution of the activity distribution with a scatter distribution function f : $S = P * f$. Rearranging these equations leads to $P = P_m - P * f$, requiring an a priori knowledge of f . It is assumed that a function h , similar to f , can be derived, such that $P = P_m - P_m * h$. Furthermore, the activity distribution is considered as a superposition of line sources, which makes it possible to find the parameters for h from the study of line sources. As introduced in (8), the projections for this kind of source can be parameterized by monoexponential functions $e^{-\alpha \cdot |x| + \beta}$. For scatter correction of experimental data, we used a modified Bergström algorithm with the parameterization (12).

Scatter Components

There is no consensus in the literature on how to classify the counted coincidences. We chose a classification that distinguishes between a fixed component, depending on the machine, and a variable part, depending on the scanned object. Unlike some other studies (2,15,16), the photons were not restricted to single scattering. This led to four distinct classes (Table 1):

1. Primaries (= unscattered events).
2. Object scatter (= scattered in the phantom or in the patient).
3. Gantry scatter (= scattered in the gantry).
4. Mixed scatter (= scattered in the gantry as well as in the object).

Monte Carlo Simulations

Since a full description of the scatter process is quite complicated and computationally expensive, it is necessary to make

TABLE 1
Classification of Simulated Coincidences by Location
of Scatter Process

	Photon no. 1			
	Primary	Object	Gantry	Object + gantry
Photon no. 2				
Primary	Primary	Object	Gantry	Mixed
Object	Object	Object	Mixed	Mixed
Gantry	Gantry	Mixed	Gantry	Mixed
Object + Gantry	Mixed	Mixed	Mixed	Mixed

For example, if the first photon is unscattered (primary) and the second photon is scattered in the object (object), then the coincidence is classified as object scatter.

some simplifying approximations, while still describing the scatter process in a sufficiently exact way and keeping the code as simple as possible.

The β^+ decay is simulated by two back-to-back photons, each with 511 keV, neglecting the positron range (2–3 mm) and the small noncollinearity of the photon pairs ($\pm 0.5^\circ$). Moreover, we restricted the simulation to Compton and Rayleigh scattering, which are the predominant interactions the photons undergo at the energy considered (14). We did not simulate the scatter in the detector crystals, because this affects neither the phantom nor the gantry scatter according to our definitions. An incident photon is treated as detected when it hits a detector crystal and has a minimum pathlength through the detector of 10 mm. The discussed approximations lead to a systematic error smaller than 3%. To compare the simulated data with the experimental data, we took the detector resolution into account by a convolution of the simulated data with a Gaussian-shaped resolution function (FWHM: 4.8 mm, as estimated from experimental data).

The simulations were performed on a DEC AXP 3000/400 workstation (Digital Equipment Corp., Maynard, MA). Our MC code, based on the program EGS4 (13), describes the geometry of the PET scanner by cylinders and planes. For each simulation, we calculated 10^9 histories, leading to running times of 20 to 200 hr, depending on the phantom geometry and the activity distribution. To examine how different energy thresholds influence the scatter components, we set three energy cutoffs (200 keV, 380 keV and 450 keV). To check the independence of the simulations from the random number generator, we also performed some runs with a second random number generator. The deviations between the results were smaller than 0.5%. To compare the simulated images with the measured images, it was necessary to include an attenuation correction in the MC simulations.

Experimental

Transmission data were obtained for attenuation correction of the emission data, reconstruction of the spatial distribution of the attenuation coefficient, and use in the convolution-subtraction scatter correction algorithm (12). The transmission scans were performed with a rotating Ge-68 rod source (17).

The radioactive line sources were produced by neutron activation of copper wires (0.6 mm thick, 7 cm long) in the research reactor of our institute. Activities were between 30 MBq and 200 MBq of ^{64}Cu at the beginning of data acquisition. The activated copper wires were placed in stainless steel tubes with 0.45-mm wall thickness and 1.6-mm outer diameter. This proved to be sufficient to stop all the positrons within the steel tube.

The homogeneous activity distributions were obtained by dispersing ^{18}F -labeled 2-deoxy-2-fluoro-D-glucose in water-filled cylinders. The activity concentrations ranged from 30 kBq/ml to 350 kBq/ml at the beginning of the data acquisition period.

Since for all clinical studies the lower energy threshold of our PET system is set to 200 keV, the same setting was used for our experiments.

RESULTS

Scatter Distribution Functions

The scatter distribution functions for a simulated line source in the center of a water-filled cylinder are shown in Figure 1A. Figure 1B demonstrates how the shape of the projection changes when the line source is moved out of the center of the tomograph. The total amount of counted coincidences remains almost constant. However, the short wing is lifted, leading to a flattened slope of the monoexponential, whereas the long wing is lowered, with a steeper slope of the monoexponential.

In the projections, the gantry scatter is closely located around

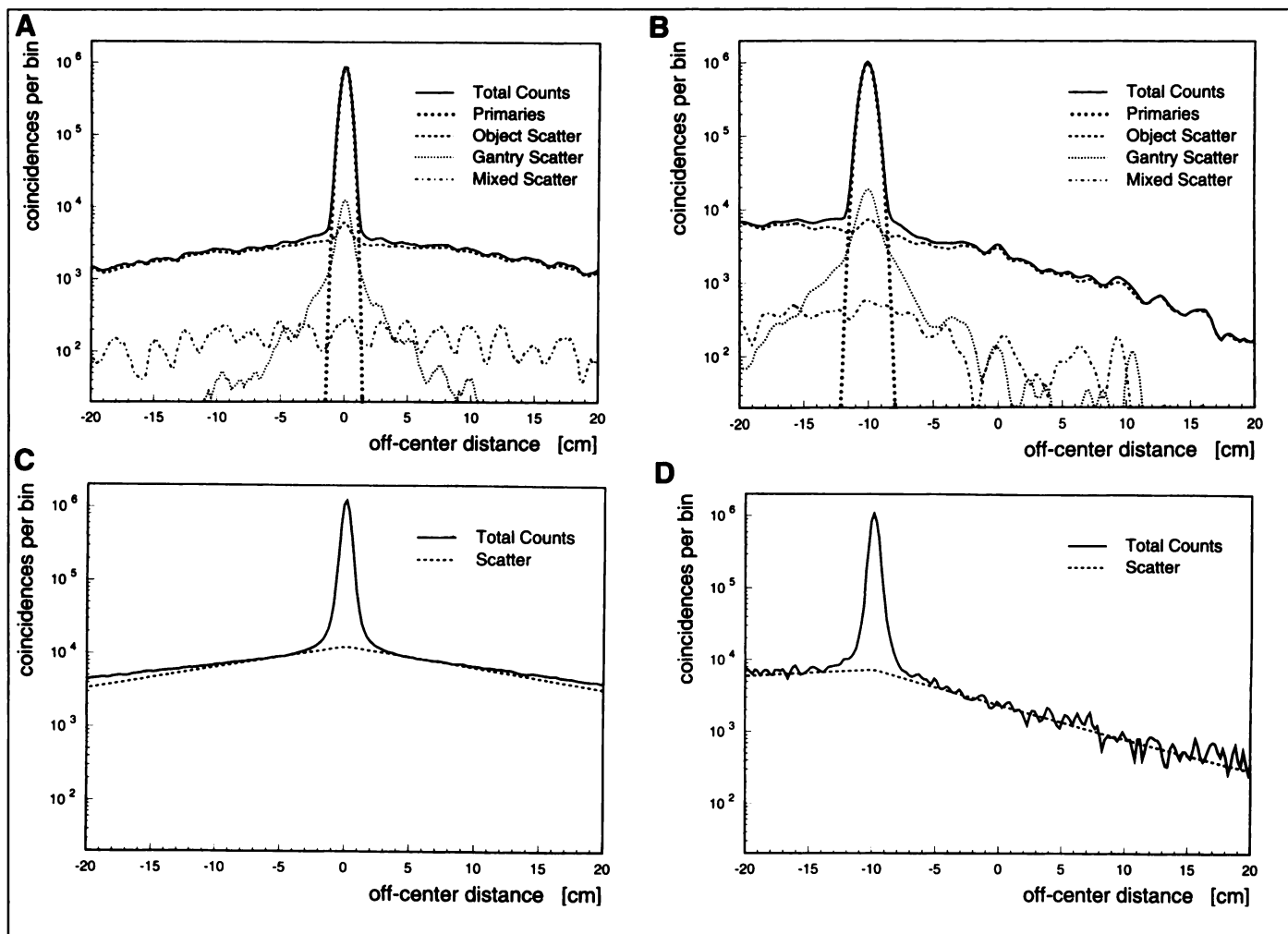


FIGURE 1. Projections of an axial ^{64}Cu line source in a water-filled cylinder ($R = 15$ cm, direct slice). (A) and (B) represent data from the MC simulations. (C) and (D) represent the corresponding experimental data. In (A) and (C), the source was placed in the center of the phantom. In (B) and (D), the source was moved 10 cm out of the center.

the source position, whereas the object scatter is smeared over the whole field of view and is well parameterized by a monoexponential function. The mixed scatter has nearly the same distribution as the object scatter, but with a smaller amplitude. This holds both for symmetric (Fig. 1A) and asymmetric (Fig. 1B) activity distributions.

Figures 1C and 1D show the corresponding measured projections for the ^{64}Cu line source in the water-filled cylinder phantom. The scatter distribution as calculated by the convolution-subtraction scatter correction algorithm is plotted as well. Table 2 compares the slopes of the scatter wings of the MC calculations with those of the experiments. The data are in excellent agreement, leading to the same parameterization of the scatter distribution functions.

TABLE 2

Parameter α (in m^{-1}) of $e^{-\alpha|x|+\beta}$ for Scatter Distribution Functions

	Centered		10 cm off-center	
	Left	Right	Left	Right
Monte-Carlo	6.10 ± 0.03	5.73 ± 0.04	1.90 ± 0.02	11.63 ± 0.01
Experiment	5.98 ± 0.85	5.78 ± 0.70	2.09 ± 1.92	11.96 ± 0.71

x = distance in millimeter to position of the line source in the projections.

Scatter Fractions

Table 3 summarizes the fractions of the scatter components for three different phantoms. It was observed that, for the same phantom size, the scatter fraction for a line source is always larger than that for a homogeneously distributed activity. The value for the EEC body phantom, compared to a cylinder phantom with a similar cross-section ($R = 15$ cm), is larger than that for a homogeneously distributed activity, but smaller than that for a line source. With increasing energy threshold, the scatter fraction decreases. The largest decrease is observed for the mixed scatter, the smallest for the gantry scatter.

Figure 2 shows the object scatter fraction SF in dependence of the radius R of the cylinder phantom. Obviously, $\text{SF}(R)$ increases with increasing R . To fit the data, we used the simple function $\text{SF}(R) = (1 - e^{-2mR})$. It fits the object scatter fraction of the line source (Fig. 2A) and the uniform activity distribution (Fig. 2B) reasonably well, although we made some crude simplifying assumptions by the derivation of this function.*

*We derived this simple formula for the object scatter fraction by assuming that the probability of a photon not being scattered is proportional to e^{-mx} (x : pathlength of the photon). The same is valid for the coincident photon, leading to a probability proportional to $e^{-m(x_1+x_2)}$ for both photons not to be scattered. In the case of a centered line source, the total length through the cylinder is always twice the radius R . Thus, the probability of two coincident photons being scattered is proportional to $(1 - e^{-2mR})$. After integration, all emitted directions and considering the normalization constraint that the limit for $R \rightarrow \infty$ should be 1, the fit function is $(1 - e^{-2mR})$. We simply assume the same functional dependence for the object scatter fraction of homogeneously distributed activities.

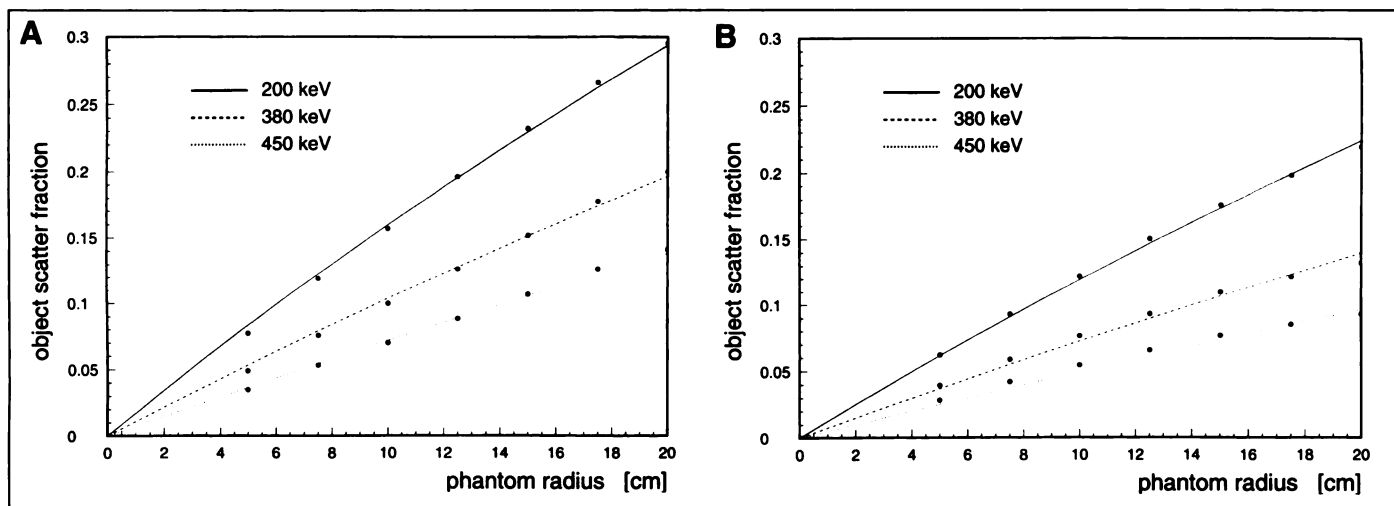


FIGURE 2. MC data from the cross-slice and fitted curves for the object scatter fraction as a function of the radius R of the cylinder phantoms for (A) a central line source and (B) homogeneous activity distribution.

Reconstructed Images

Figure 3 shows a scheme of the EEC body phantom, including the activity distribution that was used for the simulation and for the measurements as well as six images reconstructed from the MC-simulated data (with attenuation correction). The spatial reconstruction of the total counts is shown in Figure 3B. The image obtained from unscattered coincidences only is shown in Figure 3C. It contains no smearing artifacts that result from scattering and is close to the true activity distribution (Fig. 3A). The total scatter is shown in Figure 3D. How the individual scatter components contribute to the degradation of the images is demonstrated in Figures 3E–3G: the object scatter (Fig. 3E) is smeared over the whole object (note that the images are attenuation corrected), whereas the gantry scatter (Fig. 3F) is closely located around the primaries. The mixed scatter (Fig. 3G) looks like the object scatter (Fig. 3E), but the number of counts in the image is a magnitude lower, leading to a significantly decreased signal-to-noise ratio.

Figure 4 depicts the corresponding images measured with our PET scanner. The transmission scan of the EEC phantom in Figure 4A is needed for the attenuation and the scatter correction [cf. (12)]. The uncorrected scatter emission scan is shown in Figure 4B. The convolution-subtraction scatter correction algorithm was used to correct these data. The result is shown in

Figure 4C. A significant reduction of the scatter contamination is observed, demonstrating the performance of the scatter correction algorithm. Figure 4D represents the pure scatter distribution estimated by the convolution-subtraction technique. This image corresponds to the total scatter in the MC-simulated data shown in Figure 3D.

DISCUSSION

The different scatter contributions in PET have been described, showing where the photons are scattered in the scanner and how the scatter degrades the reconstructed images. We focused our study on three typical imaging situations: (a) line sources in water-filled cylinders, (b) homogeneous activity distributions and (c) the EEC body phantom. We also studied other situations (e.g., an arrangement that is comparable to a cardiac imaging situation), but these set-ups did not provide new information.

Scatter Distribution Functions

Figure 1 demonstrates that the projections are dominated in the wings by the object scatter and in the peak by the primaries. As expected, the object scatter is fairly well described by monoexponential functions. The gantry scatter, on the other hand, is closely located around the primary peak. This observation seems reasonable, since the point of interaction of a photon scattered in the gantry is closer to the detector than that of a photon scattered in the object, leading to a smaller deviation of the scattered photons. Since the gantry scatter has no significant contribution to the wings of the scatter distribution function, it can be added to the primaries.

The mixed scatter is due to photons that are first scattered in the object and then in the gantry (Table 1). Consequently, the projections look like the projections of the object scatter convolved with the gantry scatter distribution function, leading to nearly the same shape of the projections as for the object scatter, but with a smaller amplitude. Thus, the mixed scatter can also be described by monoexponential functions and can be added to the object scatter without perceptibly changing the shape of the distribution.

This discussion remains valid, when the line source is shifted out of the symmetry center. The amplitude of the short side of the projection, compared to that of the symmetrical case, is increased, since the pathlength of the photons through the phantom becomes shorter, whereas the amplitude of the long side is decreased, due to a longer pathway through the absorb-

TABLE 3
Primaries and Scatter-to-Total Fractions (%)
(Cross-Slice, MC-Simulated Data)

Phantom	Threshold	Primaries	Object Scatter	Gantry Scatter	Mixed Scatter
A	200 keV	70.9	23.2	3.5	2.4
	380 keV	80.7	15.2	2.9	1.2
	450 keV	86.6	10.7	2.2	0.5
B	200 keV	76.5	17.6	3.9	2.0
	380 keV	84.9	11.0	3.1	1.0
	450 keV	89.5	7.7	2.3	0.5
C	200 keV	74.4	19.9	3.6	2.1
	380 keV	83.3	12.7	3.0	1.0
	450 keV	88.5	8.8	2.2	0.5

A = Copper-64 line source, centered in a water-filled cylinder phantom ($R = 15$ cm); B = homogeneous activity distribution in the same cylinder; and C = homogeneous activity distributions in the EEC body phantom (Fig. 3A).

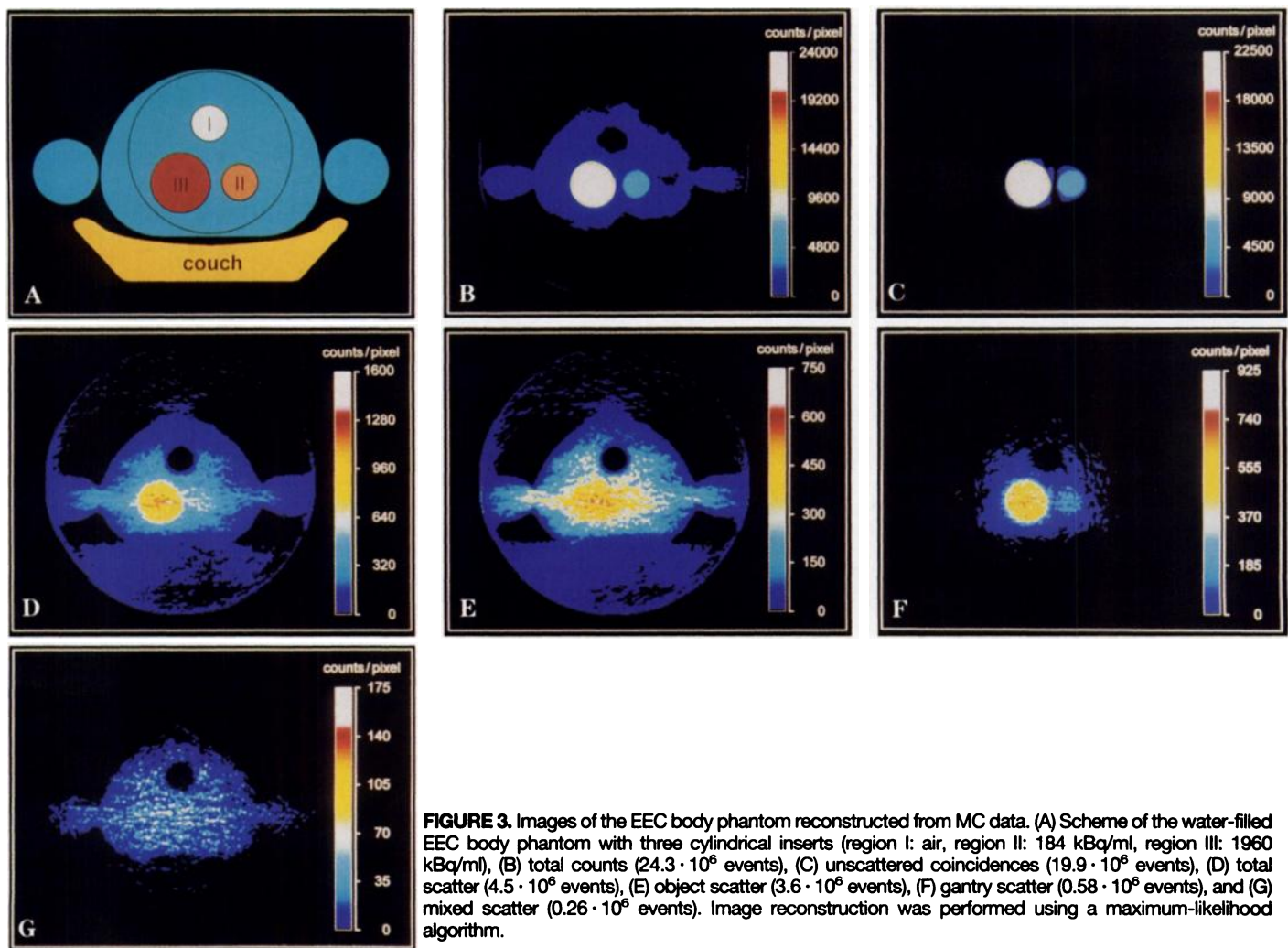


FIGURE 3. Images of the EEC body phantom reconstructed from MC data. (A) Scheme of the water-filled EEC body phantom with three cylindrical inserts (region I: air, region II: 184 kBq/ml, region III: 1960 kBq/ml), (B) total counts ($24.3 \cdot 10^6$ events), (C) unscattered coincidences ($19.9 \cdot 10^6$ events), (D) total scatter ($4.5 \cdot 10^6$ events), (E) object scatter ($3.6 \cdot 10^6$ events), (F) gantry scatter ($0.58 \cdot 10^6$ events), and (G) mixed scatter ($0.26 \cdot 10^6$ events). Image reconstruction algorithm.

ing medium. The wings of the scatter distribution are still well parameterized by monoexponentials, but now with different parameters for the left and the right side.

Our data reveal that the amount of multiple scatter is at least 2%–8% of the scattered photons, which is already the contribution from the mixed scatter. This figure does not include the multiple scattered photons that are included in the object and gantry scatter. The idea of several articles is to consider the multiple scatter by rescaling the single scatter component. This approach seems to be confirmed by our MC calculations. Obviously, a rescaling does not change the shape of the different scatter components.

The simulated and measured data are in excellent agreement, demonstrating that the parameterization of the scatter distribution functions can also be found by the MC simulations (Table 2) and that the convolution-subtraction method also works for large objects like the abdomen of a patient.

Scatter Fractions

The higher scatter fraction for a line source centered in the cylinder compared to a homogeneous activity distribution in the same cylinder is explained by the fact that, for a line source, the photons always must travel the maximum path-length through the phantom, which is not the case for a homogeneously distributed activity. The activity distribution in the EEC body phantom can be considered as a mixture of both components. Consequently, its scatter fraction is between the two extremes.

An increase of the energy threshold reduces the number of registered scattered coincidences, but it also decreases the

sensitivity of the system, leading to a reduced number of true coincidences (18). As expected, the largest effect is achieved for multiple scattered photons and photons that are scattered under a large angle. Therefore, the mixed and object scatter show a stronger dependence on the energy threshold than the gantry scatter (Table 3).

Since the function $SF(R) = (1 - e^{-2mR})$ fits the object scatter fraction for line sources and uniform activity distributions in cylindrical shaped objects reasonably well (Fig. 2), it allows an estimation of the amount of object scatter for simple activity distributions. According to our definition (Table 1), primaries and gantry scattered photons are indistinguishable until they enter the collimator, since they are both *not* scattered in the object. This means that the gantry scatter is correlated with the primaries and not with the object scatter, which was already assumed in some earlier studies (3,19). Therefore, the gantry scatter becomes relevant for small objects, such as small animals, when the object scatter fraction goes to zero.

Reconstructed Images

As shown in Figures 3 and 4, the images obtained by the MC simulations and the measurements are in good agreement. No significant difference is visible. With the MC technique, the experimental scatter distribution (Fig. 4D) can be split into the three components: object scatter (Fig. 3E), gantry scatter (Fig. 3F) and mixed scatter (Fig. 3G). These images provide a visual impression of how the different scatter components influence the image. The contribution of the scatter components to the images is exactly as one would deduce from the distribution of the scatter in the projections (Fig. 1). The true coincidences and

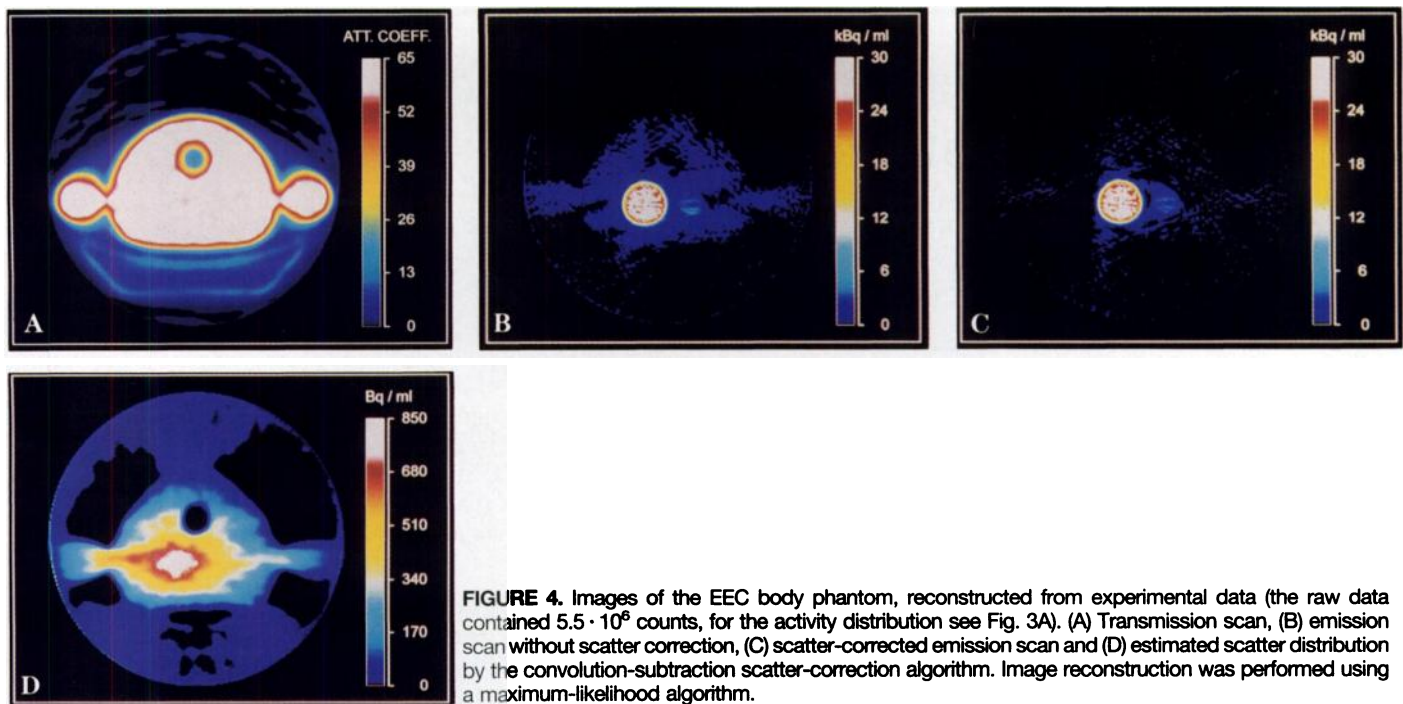


FIGURE 4. Images of the EEC body phantom, reconstructed from experimental data (the raw data contained $5.5 \cdot 10^6$ counts, for the activity distribution see Fig. 3A). (A) Transmission scan, (B) emission scan without scatter correction, (C) scatter-corrected emission scan and (D) estimated scatter distribution by the convolution-subtraction scatter-correction algorithm. Image reconstruction was performed using a maximum-likelihood algorithm.

the gantry scatter produce similar pictures (Fig. 3C and 3F), with a reduced spatial resolution in the gantry scatter image. The object and the mixed scatter also lead to similar maps, but with a lower signal-to-noise ratio for the mixed scatter since it has significantly less counts.

The images reveal that the main cause for image degradation is object scatter, whereas gantry scatter plays only a minor role. For an accurate activity quantification, it is thus mandatory to know the object scatter, whereas the gantry and mixed scatter can be estimated from the primaries and object scatter, respectively.

CONCLUSION

In contrast to the experiment, MC simulations allow a clear differentiation of the various scatter components and make it possible to illustrate their contributions in the reconstructed images. The MC-simulated data validate the frequently used convolution-subtraction algorithm and, moreover, make it possible to derive the necessary parameters for the scatter kernels. This allows for future applications to determine the scatter kernels with MC simulations only, which will be of increasing importance for three-dimensional PET systems. The large amount of point and line source measurements, which will dramatically increase in the more complex situation of a fully three-dimensional PET system, can be reduced to a minimum set of experiments needed to verify the simulated data experimentally.

Work is in progress to extend the described techniques to fully three-dimensional PET systems to derive the parameters for scatter kernels and to obtain quantitative data for an optimum scatter-correction algorithm in three-dimensional PET.

ACKNOWLEDGMENTS

We thank the personnel of the reactor, cyclotron and radiochemistry group for providing the radioactive material used in this study. The expert technical assistance of H. Trojan and the support of Dr.

J. Doll with image reconstruction are gratefully acknowledged. We thank Dr. H. Ostertag for critical review of the manuscript and Dr. W. Kübler for valuable discussions.

REFERENCES

1. Bellemann ME, Brix G, Strauss LG, et al. Scatter correction for quantitative PET measurement of the cytostatic agent 5-[fluorine-18]fluorouracil in liver tumors. *Radiology* 1994;193:131.
2. Logan J, Bernstein HJ. A Monte Carlo simulation of Compton scattering in positron emission tomography. *J Comput Assist Tomogr* 1983;7:316–320.
3. Bentourkia M, Msaki P, Cadorette J, Lecomte R. Assessment of scatter components in high-resolution PET: correction by nonstationary convolution subtraction. *J Nucl Med* 1995;36:121–130.
4. Bentourkia M, Msaki P, Cadorette J, Lecomte R. Energy dependence of scatter components in multispectral PET imaging. *IEEE Trans Nucl Sci* 1995;42:138–145.
5. Ziegler SI, Kuebler WK. Monte Carlo simulation of the scatter component in small animal positron volume-imaging devices. *Z Med Phys* 1993;3:83–87.
6. Barney JS, Rogers JG, Harrop R, Hoverath H. Object shape dependent scatter simulations for PET. *IEEE Trans Nucl Sci* 1991;38:719–725.
7. Thompson CJ, Moreno-Cantu J, Picard Y. PETSIM: Monte Carlo simulation of all sensitivity and resolution parameters of cylindrical imaging systems. *Phys Med Biol* 1992;37:731–749.
8. King PH, Hubner K, Gibbs W, Hooloway E. Noise identification and removal in positron imaging systems. *IEEE Trans Nucl Sci* 1981;28:148–151.
9. Bergström M, Eriksson L, Bohm C, Blomqvist G, Litton J. Correction for scattered radiation in a ring detector positron camera by integral transformation of the projections. *J Comput Assist Tomogr* 1983;7:42–50.
10. Holte S, Ostertag H, Kesselberg M. A preliminary evaluation of a dual crystal positron camera. *J Comput Assist Tomogr* 1987;11:691–697.
11. Guzzardi R, Bellina CR, Knoop B, et al. Methodologies for performance evaluation of positron emission tomographs. *J Nucl Biol Med* 1991;35:141–157.
12. Hoverath H, Kuebler WK, Ostertag HJ, et al. Scatter correction in the transaxial slices of a whole-body positron emission tomograph. *Phys Med Biol* 1993;38:717–728.
13. Nelson WR, Hirayama H, Rogers DWO. The EGS4 code system. *SLAC-Report-265*. Stanford, CA: Stanford University; 1985.
14. Particles and fields. Part II: review of particle properties. *Phys Rev D* 1992;45:22.
15. Ollinger JM, Johns GC, Burney MT. Model-based scatter correction in three dimensions. In: *IEEE Conference Record*. Orlando, FL: IEEE; 1992:1249–1251.
16. Ollinger JM, Johns GC. Model-based scatter correction for fully 3D PET. In: *IEEE Conference Record*. San Francisco, CA: IEEE; 1993:1264–1268.
17. Ostertag H, Kübler WK, Doll J, Lorenz WJ. Measured attenuation correction methods. *Eur J Nucl Med* 1989;15:722–726.
18. Ollinger JM. The effect of energy threshold on image variance in fully 3D PET. In: Erangate P, Amans JL, eds. *Three-dimensional image reconstruction in radiology and nuclear medicine*. Dordrecht: Kluwer; 1996:269–276.
19. Links JM. Scattered photons as “good counts gone bad”: are they reformable or should they be permanently removed from society? [Editorial]. *J Nucl Med* 1995;36:130–131.